Experimental Mechanics manuscript No.
(will be inserted by the editor)

Impact Failure of Planetary Materials:

Lateral Field Ejecta Measurements using Particle Image Velocimetry

James D. Hogan · John G. Spray · Robert J. Rogers · Gregory Vincent · Markus Schneider

Received: / Accepted:

Abstract The dynamic fragmentation of a fine grained granitoid material has been examined. Target thicknesses ranged between 7 to 40 mm and impact energies 10 to 2,500 J. Combined particle image velocimetry and image enhancement techniques are introduced and have been used to measure the size and velocity of material ejected laterally from the rear of the target. Non-dimensional groups were formed and fitted with coefficients to predict median values of the distribution of mass and kinetic energy among radial distance, R, from the impact centre, ejecta velocities, v, and ejecta lengths, L. The statistics are well correlated with increasing non-dimensional impact energy (positive correlation for radial distance and velocity, and negative correlation for ejecta length).

Median values were used to collapse cumulative distributions, and non-centred gaussian fits were used to describe these curves. Approximately 85% of the total mass and kinetic

J.D. Hogan
Hopkins Extreme Materials Institute, the Johns Hopkins University, Baltimore, Maryland 21218, USA
Tel.: 410-516-7794
E-mail: jd.hogan@jhu.edu

J.G. Spray
Planetary and Space Science Centre, University of New Brunswick, Fredericton, New Brunswick E3B 5A3, Canada

R.J. Rogers
Department of Mechanical Engineering, University of New Brunswick, Fredericton, New Brunswick E3B 5A3, Canada

G. Vincent
ISL, 5 rue du Général Cassagnou, 68300 Saint-Louis, France

M. Scheider
ISL, 5 rue du Général Cassagnou, 68300 Saint-Louis, France

energy is captured between $R/R_{50\%}$=0.3 to 2, $v/v_{50\%}$=0.3 to 2, and $L/L_{50\%}$=0.2 and 3. This data facilitates a better comparison among a wide range of test conditions, especially when attempting to extrapolate principal features of impacts into brittle materials at higher velocities. The ejecta tracking techniques and methodologies can be used to improve current impact testing and computer modelling.

Keywords particle tracking velocimetry · dynamic fragmentation · brittle materials · planetary materials · brittle fracture · ejecta measurements

1 Introduction

The impact response of brittle materials is complex due to multi-axial stress states experienced by the body under the high strain rate loading. Tensile stresses promote fracture of the body, while shear stresses lead to cascading thermal and plastic behaviour [1]. Secondary effects of fragmentation, such as plasticity and acoustic emission, are dependent on material type and properties [2,3], and the distribution of flaws [4]. For example, glasses are extremely brittle and exhibit little plastic deformation [5], while more ductile natural mineral phases, such as biotite, can exhibit more elastic and plastic behaviour [6]. A better understanding of the dynamic fragmentation of brittle materials during impact will facilitate improved understanding of impact cratering and associated ejecta phenomena [7].

Typically, a two-dimensional [8,9] view is taken using a viewing plane that includes the impact direction to allow visualization of the fastest moving fragments ejected from the rear of the solid targets [10]. This viewing plane is termed the 'streamwise' plane, which also includes one component of the lateral direction motion. Understanding streamwise material ejection is important in interpreting the origins of material ejected from low-speed colliding objects and in mitigating the threat posed by sprayed materials during impact into brittle materials. Measurements of the lateral ejecta field is investigated here for a tonalitic granitoid (a natural rock comprises of quartz, plagioclase, and orthoclase, plus minor opaque minerals).

Experimental measurements of ejecta velocity have primarily utilized vertical impacts to simulate impact cratering processes into granular [11,9] and analog lunar and asteroid

materials [12]. Added effects of fracture, such as length scales (e.g., target thickness, grain size) and the role of mineral composition, must be considered when solid planetary material is used. Ejecta velocity measurements have been determined in the past using a laser sheet to illuminate fragments captured by high-speed camera [13, 14] and by tracing vector fields onto photographs [15]. More recently, particle image velocimetery [16] and particle tracking velocimetry [8, 10, 17, 18] have been used to perform ejecta velocity measurements. In all cases, these types of experiments are challenging to perform.

The lateral ejecta field expansion during impact into finite, solid planetary materials is investigated in the current paper. Particle image velocimetry techniques are used to determined ejecta velocities and image analysis is used to determine ejecta lengths. The distribution of mass and kinetic energy among ejecta velocity and length is examined in this submission. Known ejecta spatial coordinates and velocities are used to retract ejecta to zero time. The distribution of mass and kinetic energy are investigated for radial distance from the impact centre (i.e., centre of the target). Bulk and micro-scale failure features of the targets are also characterized. Non-dimensional scaling laws are developed and implications discussed. This investigation is a part a broader study by Hogan et al. [1, 10, 17–19] on (1) fragmentation, (2) material ejection and (3) micro-scale energy dissipation mechanisms during impact into rocky targets. In these studies, ejecta measurements taken from side views were made for three types of granitoid materials and gabbro, and combined to develop non-dimensional scaling laws predicting the distributions of mass, momentum and kinetic energy among ejecta length and velocity. This method can be computationally expensive for very cluttered debris fields. Particle tracking velocimetry, a different technique than the one used here, was used to perform those measurements.

2 Experimental Setup and Analysis Methods

The impact tests were performed using an electromagnetic railgun launch system at the French-German Research Institute of Saint-Louis (ISL), France. A tonalitic granitoid (tonalite) was used as the target material for thicknesses of 7 to 40 mm, and impact energies of 12 to 2,500 J for a total of 41 experiments (Table 1). The targets were 120 mm by 120 mm. Pho-

tographs of the target materials and the aluminum projectile used as the impactor (65 g) are shown in Figure 1. Targets were sandwiched at 5 mm around their periphery using 5 mm thick steel plates.

2.1 Ejecta Tracking Methods

A Photron APX Ultima video camera filming at a 8 kHz frame rate captured images of material ejected at the rear of the targets. Two high-powered lamps were used to back-illuminate the particles on a black background (Figure 2). Proper lighting and contrast between fragments and background were critical to enhancing the images for successful velocity and size measurements.

Ejecta velocity measurements were performed by projecting an enhanced still image of fragments onto a velocity field obtained using particle image velocimetry (PIV). A custom program written in Matlab [20] was used to process the data. Image processing involves background subtraction and enhancement within the interrogation window to make the ejecta more distinguishable. The area of interrogation are for the 30 mm case at an impact energy of 735 J is shown in Figure 2a. The size of the window is determined by the expansion rate of the debris during the earliest stages of material ejection. Image enhancement is performed in two stages. The first stage involves identifying and enhancing fragments $>$5 mm. These fragments are subtracted from the image and the second stage is applied. The second stage involves descretizing the interrogation area and performing the sub-enhancement of cluttered regions. Fragments are identified as brighter areas in these sub-regions. Once the images are enhanced, fragment sizes and their centroids are determined. Estimates of fragment masses are obtained by multiplying the projected area of the ejecta with the minor axis dimension [1] and density. Ejecta smaller than 1 mm (area of three pixels determined by resolution of the camera) are filtered out.

Fragment centres are projected onto the velocity field at time t_i (obtained using PIV). PIV is a whole-field, non-intrusive measurement technique, where the velocity field is measured by recording the displacement of ejecta for gridded regions (termed cell). For PIV in

[1] Taken as the perpendicular axis to the largest spanning dimension.

fluids, the flow is seeded with small, similar density particles and the flow field is illuminated by a laser. Here, illuminated ejecta are used to perform the velocity measurements. In some cases a cell may contain more than one ejecta.

The interrogation window is gridded and the velocity at the centre of each cell grid is determined as follows: consider a particle in the flow field (Figure 3); the particle at position x_t is tracked over two time instants (left and centre images) using cross correlation of the consecutive images. The displacement, Δs, of the field is then estimated (right image) and the cell velocity obtained (equal to displacement/time). This is repeated for all cells to determine the x and y components of the velocity field for all time. Post-processing of the gridded velocity field involves the spatial averaging of erroneous vectors (determined as being outside a standard deviation range from adjacent vectors).

Individual ejecta velocities are obtained using a weighted average of their centroid distance from the adjacent cell centre velocities. The momentum and kinetic energy of individual ejecta are then estimated. Subsequent measurements are taken following further expansion of the field so as to not record the same ejecta twice. This is coupled with applying an upper bound on ejecta velocities in subsequent frames. Shown in Figure 2b is the gridded PIV vector field (blue arrows) contour, with projected ejecta vectors (red arrows) obtained by using image enhancement techniques to Figure 2a. This if for the 30 mm case at an impact energy of 735 J.

2.2 Non-Dimensional Groups and Ejecta Scaling

Input conditions and dimensions of: projectile radius (a: m), and impact energy[2] (KE: kg m^2 s^{-2}), and target thickness (t: m), density (ρ: kg m^{-3}), yield strength (Y: kg m^{-1} s^{-2}) and fracture toughness (K_c: kg m$^{-1/2}$s^{-2}) are used with the Buckingham Pi Theorem [21] to develop non-dimensional groups. These groups are developed to view the experimental results in a broader context. They are needed because analytical solutions are non-existent for the experimental results under consideration.

[2] Defined as the change in projectile kinetic energy (i.e., before and after impact if perforation occurs).

Projectile radius, a, is chosen as an important input parameter because its size affects the size of the contact zone which, in turn, affects the size of the material spalled from the target rear. The projectile radius is a=10 mm. Target thickness, t, is considered influential during the fragmentation and ejection of the target material. A kinetic energy term, KE, can be related to fragmentation and ejection processes during impact events. Shown in Table 1 is a summary of target thicknesses and impact energies for all experimental trials.

Target density (ρ), yield strength (Y) and fracture toughness (K_c) are important controls during the fracture of brittle materials. These are common material properties used in the theoretical predictions of fragment size (e.g., Grady [22], Zhou et al. [23]). Values are taken as ρ=2800 kg/m^3, Y=148 MPa, and K_c=1.8 MPa $\sqrt{m}$ [24].

According to the Buckingham Pi Theorem [21], three non-dimensional groups can be formed with six independent variables (projectile radius, impact energy, and target thickness, density, yield strength and fracture toughness) and three units (length, mass, and time). Projectile radius a is chosen as the characteristic length ($L^\star$) term, ρa^3 the characteristic mass ($M^\star$) term and $\rho^{1/2} a\ Y^{-1/2}$ as the characteristic time ($T^\star$) term. The resulting non-dimensional groups are:

$$KE^\star = \left(\frac{KE}{Y\ a^3} \right) \tag{1}$$

$$K_c^\star = \left(\frac{K_c}{Y\ a^{1/2}} \right) \tag{2}$$

and

$$t^\star = \left(\frac{t}{a} \right) \tag{3}$$

The form of the non-dimensional fit is thus:

$$aKE^{\star b} K_c^{\star c} t^{\star d} \tag{4}$$

where a, b, c, and d are fitted coefficients obtained using a least-squares process to predict key experimental results:

1. L: ejecta length (m).

2. R: radial distance from the impact centre at zero time. Ejecta are retracted to time zero using their known x and y velocities at the (x,y) coordinate at time, T (e.g., x(T=0)= x(T)-v_x(x,T)).
3. v: ejecta velocity (m/s).

Coefficient-fitted non-dimensional groups yield semi-empirical models of experimental results: $vT^\star/L^\star$, $L/L^\star$ and $R/L^\star$.

3 Experimental Results

3.1 Bulk-Scale Failure Characteristics

Preliminary consideration of target failure is provided to characterize bulk-scale failure processes and to determine an image reference for ensuing ejecta measurements. Shown in Figure 4 are high-speed video images for the 30 mm thick tile at impact energies of (a,b) 286 J, (c,d) 993 J, and (e,f) 2127 J. Images on the left are taken a few frames after impact and images on the right are taken during the earliest stages of ejecta field expansion. Times were chosen to compare early time ejection features with the three distinct impact energies. Radial cracks emanate from projectile hexagonal vertices (projectile outline is highlighted in yellow in Figure 4a). The vertices serve as stress concentration points. Highlighted near the projectile in the figure is the fastest moving lateral ejecta, produced along the circumferential fracture. The intersection of the few radial and circumferential fractures form six larger plate-like fragments. The expansion of the field (in terms of shape) is symmetric, with the ejection of larger fragments being asymmetric in nature (they are ejected to the right in Figure 4b).

Increasing the impact energy from 286 J to 993 J results in an increase in radial and circumferential fracturing (Figure 4c). Fragments, including the larger ones, are ejected symmetrically and the size of the ejecta becomes noticeably smaller (Figure 4d). The radial and circumferential fracturing increases further for an impact energy of 2127 J, and fragments further decrease in size (Figure 4e and f). In all cases, when allowed to expand, ejecta are

discernible on the black target holder background, allowing them to be isolated in the image, and their size and velocity measured.

An example of the debris field shape and post-experiment state of the targets is shown in Figure 5 for a target thickness of 30 mm at an impact energy of 993 J. The video image is a side-view of the material ejected from the rear of the target and is taken parallel with the direction of the incoming projectile (projectile travels right to left in Figure 5a). The material of interest in the current study is that with non-zero lateral velocity. The material that is ejected first (material furthest to the left) is larger than the crushed material following behind it. The faster moving larger ejecta (i.e., those $>$5 mm) contain $>$80% of the total kinetic energy and the total mass of the ejecta [8]. These ejecta are more easily measured because they are not cluttered with finely crushed fragments.

Shown in Figure 5b is a photograph of the target post-impact for a thickness of 30 mm and impact energy of 993 J. No target perforation by the projectile occurred when $t > 10$ mm. In all cases, the elastic, or shock, wave generated at impact was responsible for fragmenting the target and expelling the material. Also shown in Figure 5b is a large thin fragment. This was found at the centre of the crater and is likely generated from spallation. This indicates that not all large fragments originate from the rear of the target. A cross-section of the target (Figure 5c) reveals multiple incipient spall planes.

3.2 Ejecta Scaling: Cratering Efficiency and the Distribution of Mass and Kinetic Energy for Radial Distance from the Impact Centre, and Relative to Ejecta Velocities and Lengths

Initially, non-dimensional groups were developed and fitted with coefficients to predict the % of target material removed during impact (termed cratering efficiency) (Figure 6). Again, coefficients are obtained using a least-squares fit of the non-dimensional groups. As expected, the amount of material ejected from the target increases for increasing impact energy (exponent for KE* of b=0.45).

The distribution of mass and kinetic energy for radial distances away from the centre of impact, R, at time zero is now considered (Figure 7). The corresponding radial distance for 50% of the mass (termed $R_{50\%mass}$) and for the 50 % of the lateral kinetic en-

ergy ($R_{50\%KE}$) normalized by the projectile radius is plotted against coefficient-fitted non-dimensional groups (Figure 7a and Figure 7b, respectively). In both cases, the radial distance increases for increasing impact energy, ranging from one projectile radius ($R/L^{\star}$=1) to approximately six projectile radii. $R_{50\%mass}/L^{\star}$ ($\propto \mathrm{KE}^{\star 0.50}$) increases at a greater rate than $R_{50\%KE}/L^{\star}$ ($\propto \mathrm{KE}^{\star 0.37}$). Similarly, $R_{50\%mass}/L^{\star}$ ($\propto \mathrm{t}^{\star -1.49}$) decreases at a greater rate than $R_{50\%KE}/L^{\star}$ ($\propto \mathrm{t}^{\star -1.07}$) for target thickness.

Corresponding cumulative distributions of mass for radial distance (M(R)) and leteral kinetic energy (KE(R)) normalized by $R_{50\%mass}$ and $R_{50\%KE}$, respectively, are shown in Figures 7c and 7d. By definition, the points pass through (1, 50). Curves collapse well under the selected normalization. Also shown in the figure (hashed line) are curve-fits of a non-centred gaussian curve-fit in the form of:

$$\%Mass, KE > R/R_{50\%i} = C_1 exp\left(\frac{-(x+x_0)^2}{2\sigma^2}\right) \tag{5}$$

where C_1 is a fitted coefficient (approximately equal to 100%), x corresponds to $R/R_{50\%}$, x_0 is the mean, and σ is the standard deviation. This function is able to fit the collapsed data well. 85% of the total mass and kinetic energy is captured between $R/R_{50\%}$=0.3 to 2.

Normalized median values for ejecta lateral velocity among mass ($v^{\star}_{50\%mass}$:Figure 8a) and kinetic energy ($v^{\star}_{50\%KE}$: Figure 8b) are plotted against coefficient-fitted non-dimensional groups. $v_{50\%mass}$ and $v^{\star}_{50\%KE}$ increase for increasing normalized impact energy and at a greater rate for mass ($v^{\star}_{50\%mass}$: $\propto KE^{\star 0.96}$ to $v^{\star}_{50\%KE}$: $\propto KE^{\star 0.78}$). Similarly, $v^{\star}_{50\%mass}$ decreases at a greater rate than for target thickness ($\propto t^{\star -2.68}$) than for $v^{\star}_{50\%KE}$ ($\propto t^{\star -2.41}$).

Cumulative distributions of mass among velocity (M(v)) and kinetic energy among velocity (KE(v)) normalized by their respective $v_{50\%}$ are plotted in Figures 8c and d, respectively. Also shown in the sub-figures are non-centered gaussian curve fits in the form of equation 5. The curves overlie well when normalized by their median values and the curve-fit provides reasonable agreement with the data. Greater than 85% of the mass and kinetic energy are contained between $v/v_{50\%}$=0.3 to 2.

Normalized medians of mass ($L_{50\%mass}$) and kinetic energy ($L_{50\%KE}$) among ejecta length are plotted against coefficient-fitted non-dimensional groups in Figure 9a and b, re-

spectively. Values decrease at a greater rate for increasing $KE^{\star}$ for ejecta kinetic energy contribution ($\propto KE^{\star -0.47}$) than for mass ($\propto KE^{\star -0.37}$), with values ranging from $L_{50\%}/L^{\star}$=1 to approximately 5 (Figure 9a and b). Values also increase at a greater rate for increasing $t^{\star}$ for ejecta kinetic energy contribution ($\propto t^{\star 0.97}$) than for mass ($\propto t^{\star 0.46}$). Corresponding normalized cumulative distributions of mass and kinetic energy for ejecta length (M(L) and KE(L)) are shown in Figures 9c and 9d with non-centred gaussian curve fits. The data collapses well and is reasonably predicted by the curve fit. Greater than 85% of the total mass and kinetic energy is contained between $L/L_{50\%}$=0.2 and 3.

3.3 Micro-Scale Damage Modes

Micro-scale energy dissipation mechanisms that occured during the dynamic fragmentation of tonalite are examined in Figure 10. Note the scales in the bottom right of each scanning electron microscope (SEM) image. For example, the 10 divisions in a respresents 500 μm. Shown in Figure 10 are examples of sub-mm fragments. Examination of their fracture surfaces reveals multiple sub-μm fragments on their surfaces (Figure 10b). These are likely generated from the abrasion of fractured surfaces following initial fragmentation. The initial fragmentation process only represents a fraction of the final number of fragments [25]. Abrasion of fractured surfaces also generates local melting (Figure 10c), which can lead to spheroid formation (Figure 10d).

Lastly, intra-fragment features are shown in Figures 10e and 10f. These fragments were mounted in resin and systematically polished to reveal intra-fragment structure. The different shades in Figures 10e and 10f represent different mineral phases (quartz, albite, biotite) under the back-scatter viewing mode, with the more dense materials appearing lighter in the image. Transgranular fracture is observed in the larger multi-phase fragments (Figure 10e), while substantial intra-fragment fracture occurs in the smaller mono-phase (albite) fragments (Figure 10f). Fractures are concentrated near the protruding edges in Figure 10f.

4 Summary and Discussion

The dynamic fragmentation of tonalite has been investigated for target thicknesses of 7 to 40 mm and impact energies of 12 to 2,500 J. Bulk-scale failure processes and the earlier stages of lateral debris field expansion are characterized. An increase in impact energy results in an increase in radial and circumferential fracturing, and a reduction in ejecta fragment size. The fastest moving ejecta in directions perpendicular to the incoming projectile were observed to originate from the outer rim during circumferential cracking. These are very few (3 to 5 fragments). The larger fragments were generated via spallation and originated from the target rear surface and along the inner surface of the Hertzian fracture cone. Incipient spallation was observed in the cross-section of the target.

Micro-scale features of fracture were also observed. Substantial sub-μm fragmentation generated through contact (abrasion) of fracture surfaces was noted. These tiny fragments represent $>$99% of the total number of fragments generated from impact [19], but account for $<$1% of the total mass (Figure 9c). The generation of melt and spheroid formation indicates local temperatures in excess of 1,000 K [7] are achieved during the fragmentation process. Substantial fracturing was observed within sub-mm fragments. These common features require improved consideration in numerical codes, as the sub-mm heat generation and dissipation likely represent a significant portion of the total energy dissipation.

Non-dimensional groups in the form of equation (4) were fitted with coefficients a, b, c, and d to predict cratering efficiency, median values for radial distance ($R_{50\%mass}$ and $R_{50\%KE}$), and ejecta velocities ($v_{50\%mass}$ and $v_{50\%KE}$) and lengths ($L_{50\%mass}$ and $L_{50\%KE}$). Cratering efficiency was found to increase $\propto KE^{\star 0.45}$. KE coefficients are in close agreement with those presented by Schmidt and Holsapple [26] of 0.47 to 0.50, and this suggests a universal dependence of the KE-coefficient for rocky materials.

The radial distance increases for increasing impact energy, ranging from one projectile radius ($R/L^{\star}$=1) to approximately six projectile radii. $R_{50\%mass}/L^{\star}$ ($\propto KE^{\star 0.50}$) increases at a greater rate than $R_{50\%KE}/L^{\star}$ ($\propto KE^{\star 0.37}$), indicating that the expulsion of target material lags the generation of ejecta mass. The distribution of mass among velocity also expands at a greater rate than kinetic energy ($v_{50\%mass}$: $\propto KE^{\star 0.96}$ to $v_{50\%KE}$: $\propto KE^{\star 0.78}$). Median values

of kinetic energy relative to ejecta length were found to decrease at a greater rate for increasing KE ($\propto KE^{\star -0.47}$) than for mass ($\propto KE^{\star -0.37}$), with values ranging from $L_{50\%}/L^{\star}$=1 to approximately 5.

Once median values were determined, they were used to normalize and collapse cumulative distributions. Curve-fits were then applied to the collapsed data in the form equation (5). This function fits the collapsed data well for all cases and can be integrated to obtain the probability density distribution forms. 85% of the total mass and kinetic energy is captured between $R/R_{50\%}$=0.3 to 2. Maxima occur at approximately $R/R_{50\%}$=5. 85% of the mass and kinetic energy are contained between $v/v_{50\%}$=0.3 to 2 and between $L/L_{50\%}$=0.2 and 3.

5 Concluding Remarks

The dynamic fragmentation of tonalite was examined for target thicknesses of 7 to 40 mm and impact energies of 12 to 2500 J. The objective was to obtain data to better understand lateral ejecta field behaviour. Particle image velocimetry and image enhancement techniques were used to obtain ejecta measurements. The distributions of mass and kinetic energy were examined for the originating radial distance from the impact point, and ejecta velocities and lengths. Non-dimensional groups were formed and fitted with coefficients to predict cratering efficiency, as well as median values for radial distance, and ejecta velocities and lengths. The statistics are well correlated with increasing non-dimensional impact energy (positive correlation for radial distance and velocity, and negative correlation for ejecta length).

Median values were used to collapse cumulative distribution curves and non-centred gaussian fits were used to describe the curves. 85% of the total mass and kinetic energy is captured between $R/R_{50\%}$=0.3 to 2, $v/v_{50\%}$=0.3 to 2 and $L/L_{50\%}$=0.2 and 3. The applicability of ejecta tracking techniques and methodology can be used to improve current impact testing. The data presented here will enable better comparisons to be made for a wide range of test conditions, especially when attempting to extrapolate principal features of impact events to planetary scales.

Bulk-scale failure processes and the earlier stages of debris field expansion were also characterized. An increase in impact energy results in an increase in radial and circumfer-

ential fracturing, and a reduction in ejecta size. The fastest moving ejecta in directions perpendicular to the incoming projectile were observed to originate from the outer rim during circumferential cracking. Substantial sub-μm fragmentation and micro-scale melting were noted. These common features require consideration in numerical codes, as the sub-mm processes likely represent a significant portion of the total energy budget.

Understanding lateral ejecta field formation (e.g., zero time location, and ejecta velocities and lengths) is important in interpreting impact events and associated ejecta deposits. Further development of models predicting mechanisms of ejecta cloud formation is critical for the development and validation of high level computation models. In particular, validation through qualitative presentation of damage patterns observed in experiments will be replaced with detailed quantification of ejecta behaviour (e.g., debris cloud formation and associated velocity-size measurements). This study provides a framework and methodologies for future studies investigating ejecta fields.

Acknowledgements This work was supported by a Natural Sciences and Engineering Research Council (NSERC) PGS-D scholarship to JDH and funding from NSERC, the Canada Research Chairs program and the Canada Foundation for Innovation to JGS. The authors would also like to thank the efforts and contributions during the experimental phase of the study of Yannick Boehrer, David Bluntzer and Philippe Baumann at ISL. Suporn Boonsue kindly assisted with the electron microscopy. This is Planetary and Space Science Centre contribution 81.

References

1. J. D. Hogan, J. G. Spray, R. J. Rogers, S. Boonsue, G. Vincent, M. Schneider, Micro-scale energy dissipation mechanisms during dynamic fracture in natural polyphase ceramic blocks, International Journal of Impact Engineering 38 (12) (2011) 931 – 939.
2. D. E. Lambert, C. A. Ross, Strain rate effects on dynamic fracture and strength, International Journal of Impact Engineering 24 (10) (2000) 985 – 998.
3. Z. X. Zhang, J. Yu, S. Q. Kou, P. A. Lindqvist, Effects of high temperatures on dynamic rock fracture, International Journal of Rock Mechanics and Mining Sciences 38 (2) (2001) 211 – 225.
4. F. Zhou, J.-F. Molinari, K. Ramesh, A cohesive model based fragmentation analysis: effects of strain rate and initial defects distribution, International Journal of Solids and Structures 42 (1819) (2005) 5181 – 5207.

5. L. B. Freund, Stability of a dislocation threading a strained layer on a substrate, Journal of Applied Mechanics, Transactions ASME 54 (3) (1987) 553–557.
6. J. D. Hogan, R. J. Rogers, J. G. Spray, S. Boonsue, Dynamic fragmentation of granite for impact energies of 6 to 28 J, Engineering Fracture Mechanics 79 (2012) 103 – 125.
7. J. G. Spray, Frictional melting processes in planetary materials: From hypervelocity impact to earthquakes, Annual Review of Earth and Planetary Sciences 38 (1) (2010) 221–254.
8. J. D. Hogan, J. G. Spray, R. J. Rogers, G. Vincent, M. Schneider, Dynamic fragmentation of natural ceramic tiles: Ejecta measurements and kinetic consequences, International Journal of Impact Engineering 58 (0) (2013) 1 – 16.
9. B. Hermalyn, P. H. Schultz, Early-stage ejecta velocity distribution for vertical hypervelocity impacts into sand, Icarus 209 (2) (2010) 866 – 870.
10. J. D. Hogan, J. G. Spray, R. J. Rogers, G. Vincent, M. Schneider, Dynamic fragmentation of planetary materials : ejecta measurements and velocity scaling during impact testing, Planetary and Space Science In Press.
11. D. Braslau, Partitioning of energy in hypervelocity impact against loose sand targets, Journal of Geophysical Research 75 (20) (1970) 3987–3999.
12. W. K. Hartmann, Impact experiments: 1. ejecta velocity distributions and related results from regolith targets, Icarus 63 (1) (1985) 69 – 98.
13. A. Piekutowski, R. Andrews, H. Swift, Studying small-scale explosive cratering phenomena photographically, Int Congr on High Speed Photogr (Photonics), 12th 97 (1977) 177–183.
14. M. J. Cintala, L. Berthoud, F. Horz, Ejection-velocity distributions from impacts into coarse-grained sand, Meteoritics and Planetary Science 34 (4) (1999) 605–623.
15. A. Fujiwara, A. Tsukamoto, Experimental study on the velocity of fragments in collisional breakup, Icarus 44 (1) (1980) 142 – 153.
16. J. L. B. Anderson, P. H. Schultz, J. T. Heineck, Asymmetry of ejecta flow during oblique impacts using three-dimensional particle image velocimetry, Journal of Geophysical Research 108 (5094) (2003) 10.
17. J. Hogan, R. Rogers, J. Spray, G. Vincent, M. Schneider, Debris field kinetics during the dynamic fragmentation of polyphase natural ceramic blocks, Experimental Mechanics (2013) 1–18.
18. J. D. Hogan, J. G. Spray, R. J. Rogers, G. Vincent, M. Schneider, Dynamic fragmentation of planetary materials: length scale quantification and semi-analytical modelling, International Journal of Impact Engineering In Press.
19. J. D. Hogan, J. A. Castillo, A. Rawle, J. G. Spray, R. J. Rogers, Automated microscopy and particle size analysis of dynamic fragmentation in natural ceramics, Engineering Fracture Mechanics 98 (0) (2013) 80 – 91.
20. Mathworks, 2013 Matlab User Manual.
21. B. R. Munson, D. F. Young, T. H. Okiishi, Fundamentals of fluid mechanics, Wiley, 1990.

22. D. E. Grady, Length scales and size distributions in dynamic fragmentation, International Journal of Fracture 163 (1–2) (2009) 85–99.

23. F. Zhou, J. F. Molinari, K. Ramesh, Analysis of the brittle fragmentation of an expanding ring, Computational Materials Science 37 (1-2) (2006) 74 – 85.

24. H. Ai, T. Ahrens, Simulation of dynamic response of granite: A numerical approach of shock-induced damage beneath impact craters, International Journal of Impact Engineering 33 (1-12) (2006) 1 – 10.

25. S. Maiti, K. Rangaswamy, P. H. Geubelle, Mesoscale analysis of dynamic fragmentation of ceramics under tension, Acta Materialia 53 (3) (2005) 823 – 834.

26. R. M. Schmidt, K. A. Holsapple, Theory and experiments on centrifuge cratering, Journal of Geophysical Research: Solid Earth 85 (B1) (1980) 235–252.

List of Tables

List of Figures

Table 1 The number of experiments, target thickness, and impact velocity and energy

Number of Experiments	Target Thickness (mm)	Impact Velocities (m/s)	Impact Energies (J)
6	7	46 to 92	66 to 262
11	10	20 to 95	12 to 280
11	20	35 to 202	38 to 1,265
7	30	96 to 284	286 to 2,500
6	40	171 to 269	906 to 2,243

Fig. 1 Photograph of the tonalite targets (left to right: 40 mm to 7 mm thicknesses) with 65 g aluminum projectile with copper brushes. The projectile is 30 mm in length.

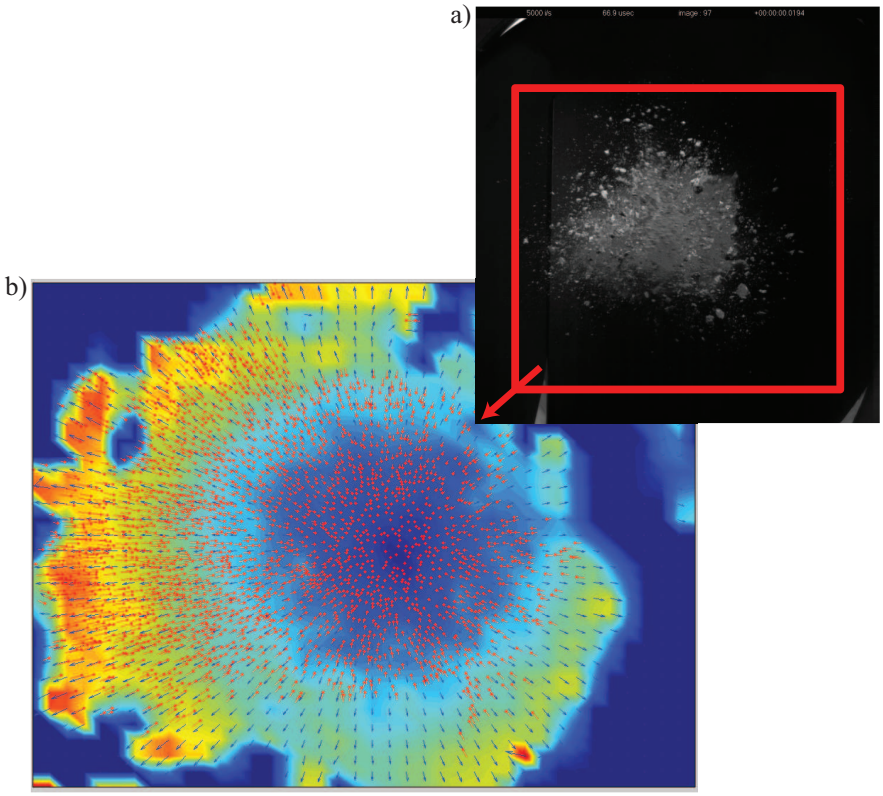

Fig. 2 (a) High-speed video image of target rear with interrogation area for 30 mm thick targets and impact energy of 735 J. (b) Vector field (blue arrows) contour from particle image velocimetry measurements with projected ejecta vectors (red).

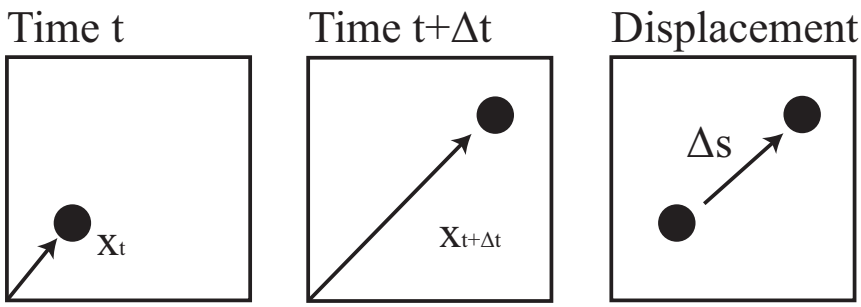

Fig. 3 Principal method for determining the cell velocity of the gridded ejecta field: the displacement of the particle over time yields the cell velocity.

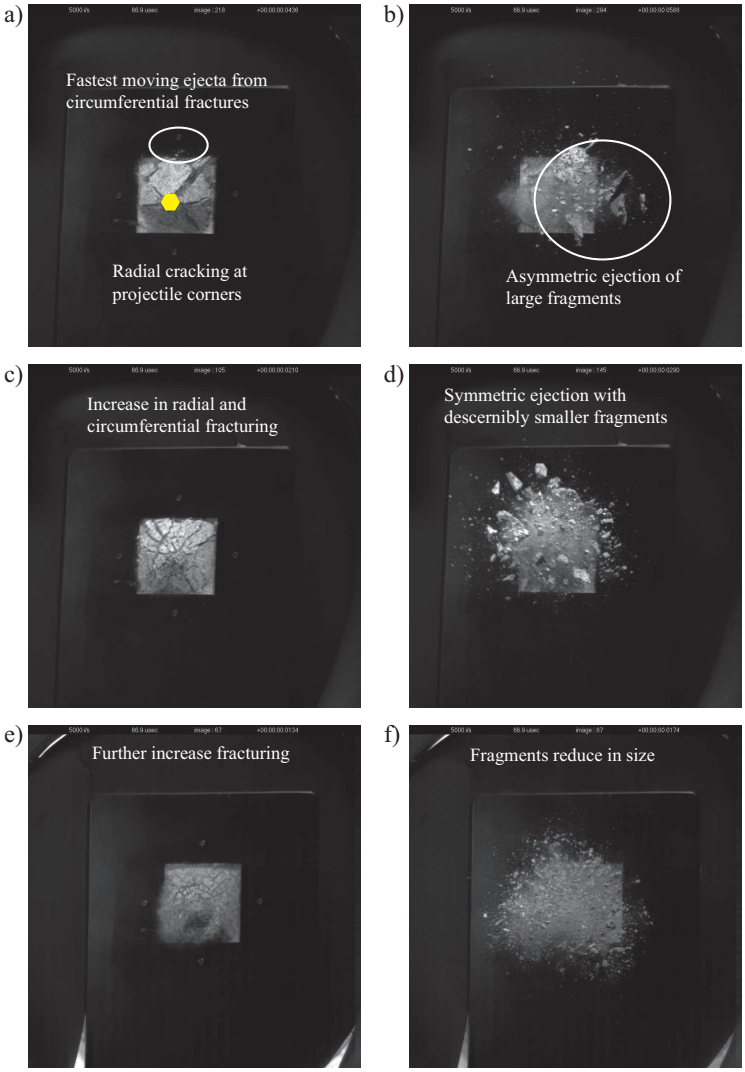

Fig. 4 High-speed video images for a target thickness of 30 mm and impact energies of (a,b) 286 J, (c,d) 993 J, and (e,f) 2127 J. The left images are a few frames after impact and the right frames have been selected to allow the earliest stages of ejecta field formation to be observed.

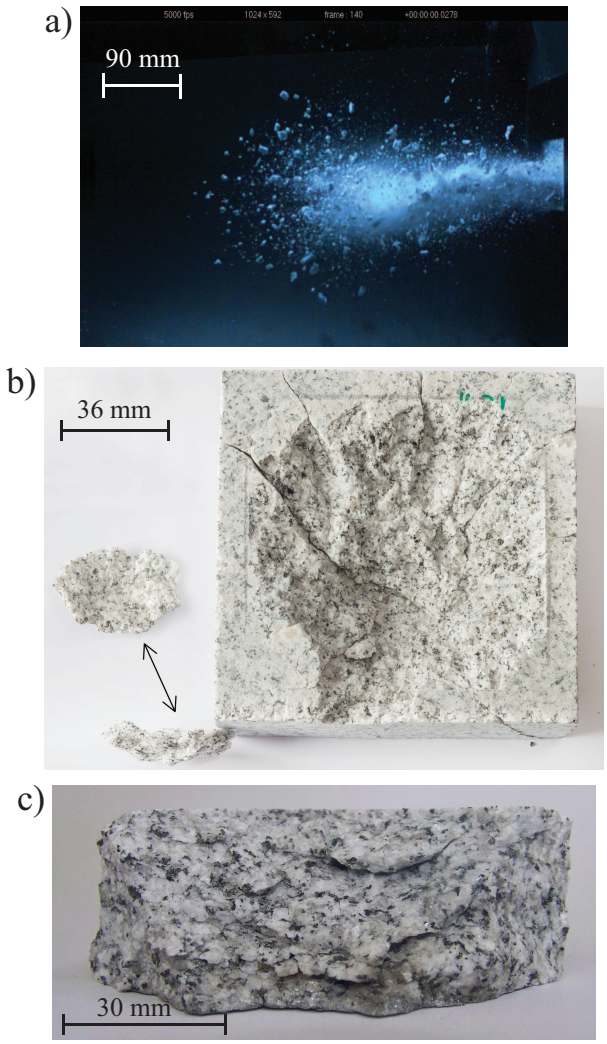

Fig. 5 30 mm at 993 J: (a) High-speed video side-view image of common ejecta field pattern viewed parallel with the fastest ejecta velocity, and photographs of (b) rear view of post-target status with rotated spalled fragment (projectile direction is travelling out of the page), and (c) cross-sectional view of target showing incipient spall planes (projectile direction travels from the bottom of the image to the top).

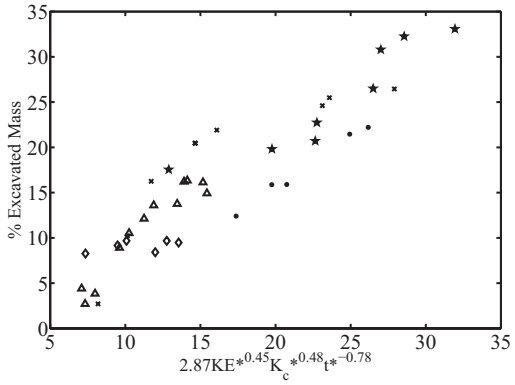

Fig. 6 The percent of excavated mass (ratio of material ejected to the original target mass) plotted against coefficient-fitted non-dimensional groups.

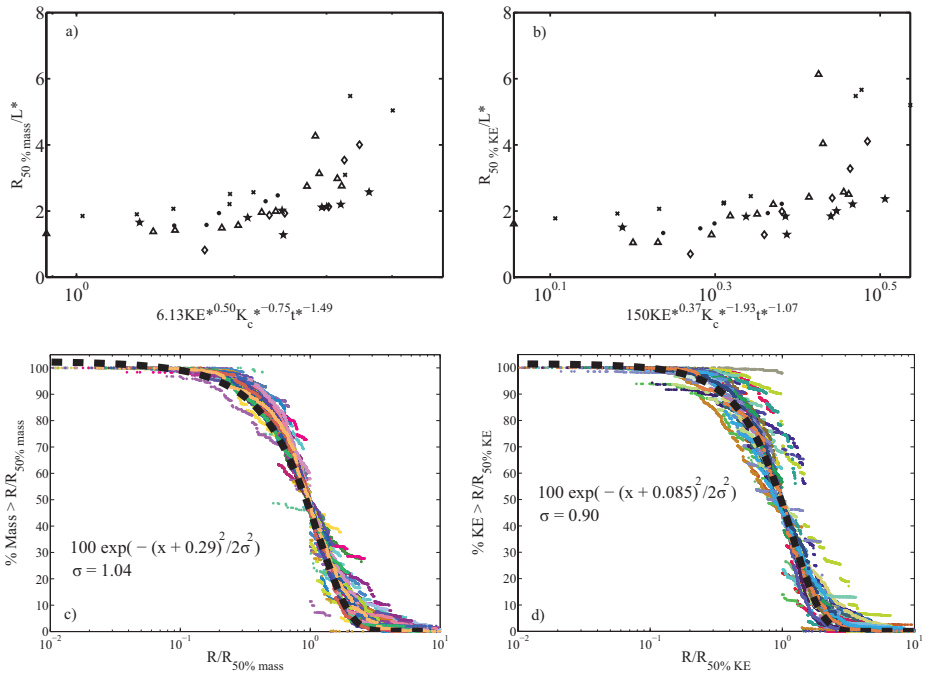

Fig. 7 Normalized 50^{th} percentiles of (a) mass and (b) lateral kinetic energy for the radial distance, R, from the impact centre. Corresponding cumulative distributions of (c) mass and (d) kinetic energy among radial distance normalized by respective 50^{th} percentiles.

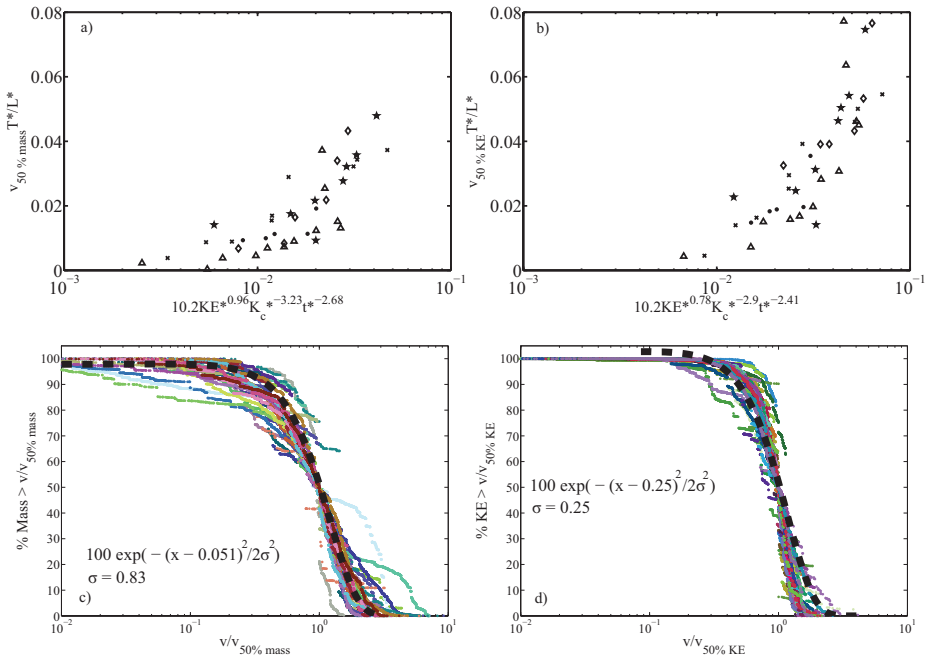

Fig. 8 Normalized 50^{th} percentiles of (a) mass and (b) lateral kinetic energy among ejecta velocities. Corresponding cumulative distributions of (c) mass and (d) kinetic energy among ejecta velocity normalized by respective 50^{th} percentiles.

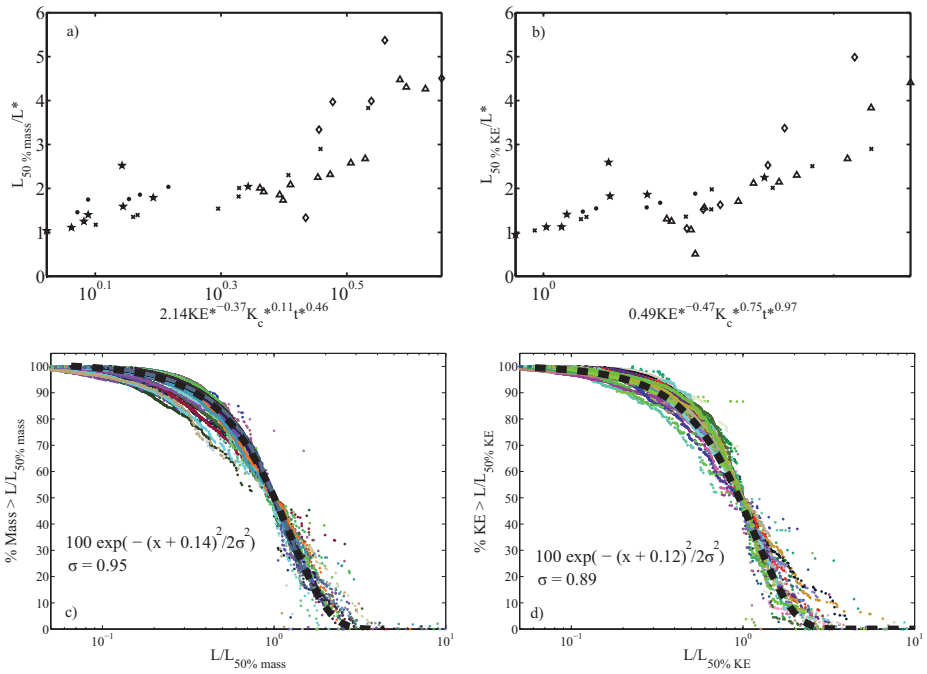

Fig. 9 Normalized 50^{th} percentiles of (a) mass and (b) lateral kinetic energy among ejecta lengths. Corresponding cumulative distributions of (c) mass and (d) kinetic energy among ejecta length normalized by respective 50^{th} percentiles.

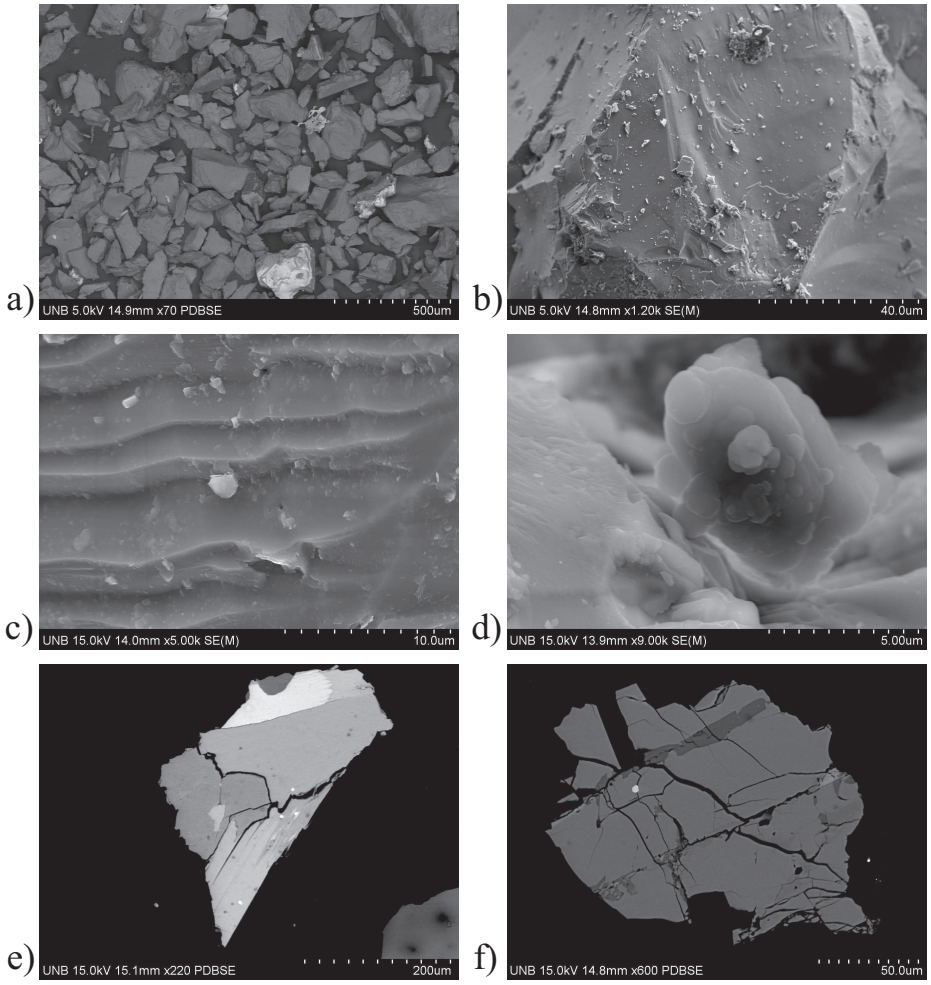

Fig. 10 Scanning electron microscope images of: (a) sub-300 μm fragments, (b) exposed fracture surface revealing the generation of micro-scale fragmentation, (c) frictional melting at grain boundaries, (d) thermal effects in the form of spheroids, (e) intra-fragment fracture along grain boundaries, and (f) significant intra-fragment fracture.